Imaging of Spontaneous Ventriculomegaly and Vascular Malformations in Wistar rats: implications for Preclinical Research

Tsang-Wei Tu, PhD[a,*], L. Christine Turtzo, MD, PhD[a], Rashida A. Williams, BS[a], Jacob D. Lescher, BS[a], Dana D. Dean, PhD[b], and Joseph A. Frank, MD, MS[a,c]

[a]Frank Laboratory, Radiology & Imaging Sciences, Clinical Center, National Institutes of Health, Bethesda, Maryland [b]Department of Environmental Science, Baylor University, Waco, Texas [c]National Institute of Biomedical Imaging and Bioengineering, National Institutes of Health, Bethesda, Maryland.

Abstract

Wistar rats are widely used in biomedical research and commonly serve as a model organism in neuroscience studies. In most cases when noninvasive imaging is not utilized, studies assume a consistent baseline condition in rats that lack visible differences. While performing a series of traumatic brain injury studies, we discovered mild spontaneous ventriculomegaly in 70/162 (43.2%) of Wistar rats that had been obtained from 2 different vendors. Advanced magnetic resonance (MR) imaging techniques, including MR angiography and diffusion tensor imaging, were utilized to evaluate the rats. Multiple neuropathologic abnormalities, including presumed arteriovenous malformations, aneurysms, cysts, white matter lesion and astrogliosis were found in association with ventriculomegaly. Postmortem micro-CT and immunohistochemical staining confirmed the presence of aneurysms and arteriovenous malformations. Diffusion tensor imaging significant decreases in fractional anisotropy and increases in mean diffusivity, axial diffusivity, and radial diffusivity in multiple white matter tracts ($p < 0.05$). These results could impact the interpretation, e.g. of a pseudo-increase of axon integrity and a pseudo-decrease of myelin integrity, based on characteristics intrinsic to rats with ventriculomegaly. We suggest the use of baseline imaging to prevent the inadvertent introduction of a high degree of variability in preclinical studies of neurological disease or injury in the Wistar rats.

Keywords

Arteriovenous malformation; Diffusion tensor MRI; Hydrocephalus; MR angiography; Ventriculomegaly; Wistar rats

[*]Send correspondence and reprint requests to: Tsang-Wei Tu, PhD, Radiology & Imaging Sciences, Clinical Center, National Institute of Health, Building 10, RM B1N256, 10 Center Drive MSC 1074, Bethesda, MD 20892. Phone: (301) 435-4488; Fax: (301) 402-4547; tut@cc.nih.gov.

INTRODUCTION

The Wistar albino rat is among the most widely used species in preclinical studies. According to the US National Library of Medicine's PubMed database, the use of Wistar rats has drastically increased in the past 2 decades; they have been used in 6.2% of rat studies indexed for 1990 vs. 30.7% for 2012. Over 109,100 research articles are associated with the key word 'Wistar rat study' in searches of PubMed to date. When a noninvasive imaging technique, e.g. magnetic resonance imaging (MRI), is not included in the evaluation or censoring of animals for brain abnormalities, such studies usually assume a consistent baseline condition in rats that lack any overt visible differences.

Congenital spontaneous hydrocephalus in Wistar rats was first reported in a study of rat embryonic development in which 1.1% of Wistar fetuses (11 of 946) were found to have abnormal head growth secondary to hydrocephalus (1). Later studies also reported high incidence rates (20%–40%) of hydrocephalus in many other albino experimental rats, including hydrocephalic Texas (H-Tx) (2), Csk: Wistar-Imamichi (WIC-Hyd) (3), Wistar-Lewis (LEW/Jms) (4, 5), Sprague-Dawley (6), Wezob (CPB-WE) and Wistar (Cpb: WU) (7) rats.

Hydrocephalus is a consequence of altered cerebrospinal fluid (CSF) flow dynamics, resulting in the enlargement of the cerebral ventricles and occasionally the subarachnoid spaces (8, 9). Overproduction of CSF in choroid plexus or obstruction of the CSF circulation pathway due to tumors, hemorrhages (10), infections (11), or congenital malformations in the CSF pathway (2-4) can also cause hydrocephalus. Congenital hydrocephalus with visible changes in skull shape and/or size is thought to be a multifactorial genetic disorder in rats (2, 3, 12). Many mutations/loci linked to hereditary hydrocephalus have been genetically identified in associated with the production of important cytokines, growth factors or molecules in cellular signal pathways active during early brain development (13-16).

In this report, spontaneous ventriculomegaly was discovered in the baseline MRI scans of Wistar rats (43.2%) used in a traumatic brain injury (TBI) study. The pattern of spontaneous ventriculomegaly discovered has not been previously reported in Wistar rats. The goal of this study was to examine the prevalence of ventriculomegaly in Wistar rats and evaluate whether the diffusion tensor imaging (DTI) parameters would be altered when including the subset of ventriculomegaly rats in an imaging study. MR techniques including T_2-weighted, T_2*-weighted, DTI and magnetic resonance angiography (MRA) (in subset of animals) were performed to diagnose the abnormality in vasculature and white matter. Postmortem micro-CT and immunohistochemistry (IHC) staining were also performed to verify the imaging findings and inspect the spontaneous anomalies in the CNS of the ventriculomegaly Wistar rats. The presence of these spontaneous ventriculomegaly patterns may be associated with abnormal vasculature, including aneurysms and arteriovenous malformations (AVM). Baseline scans are critical to exclude animals with ventriculomegaly and AVM anomalies to ensure consistent and reliable animal models of CNS diseases.

MATERIALS AND METHODS

Animal and Ventriculomegaly Rating Scale

Eight-week-old Wistar rats purchased from Charles River (n = 134, female) and Harlan Laboratories (n = 28, including 22 female and 6 male) were examined. All studies were approved by the Animal Care and Use Committee at our institution. Anatomical T_2-weighted MRI was first applied to characterize each animal's baseline condition. Each animal's baseline brain MRI studies were reviewed independently by 3 investigators assessing the scans for any ventricular dilatation, asymmetrical ventricles, aqueduct stenosis, arachnoid cysts, cyst-like lesions, hyperintense lesions and otherwise unidentified bright objects. Animals without brain anomalies on baseline MRI were considered normal. The volume of ventricles or the hyperintense CSF compartments were quantified using National Institutes of Health ImageJ (NIH, Bethesda, MD) software and normalized to the volume of brain section at the same slices for cross comparison over each animal. A CSF compartment rating scale was applied to evaluate the ventricular and cystic abnormalities. Ventriculomegaly patterns were rated at 8 anatomical locations as follows: lateral ventricles, 3rd ventricle, 4th ventricle, aqueduct, lateral recess of the 4th ventricle, white matter, enlarged basal cisterns (BC), and cerebellum, based on 30 consecutive T_2-weighted images covering the entire rat brain from the olfactory bulb to cerebellum. The details of scoring basis of CSF compartment rating scale are illustrated in Figure 1.

MRI

MRI data were acquired in vivo using a Doty quadrature coil on a Bruker 7T scanner (Bruker, Billerica, MA). Animals were anesthetized with an isoflurane/oxygen mixture (4.5%–5% for induction and 1.5%–2.0% for maintenance) to be placed in the scanner. The inhalant anesthetic was delivered to the animal through a custom-made nose cone. Throughout MR scans, warm water was circulated under the animals to keep them warm at 37°C; a steady respiratory rate was monitored using a pressure sensor (SA Instruments Inc., Stony Brook, NY), and maintained at 40 to 50 breaths/minute by isoflurane/oxygen mixture. For the baseline scan, high-resolution RARE MRI was first performed on every rat to acquire the anatomical T_2-weighted images (TR 3.8 s, TE 15 ms, RARE factor 8, field of view [FOV] 2.56×2.56 [cm], matrix 256×256, in-plane resolution 100×100 [μm] with 0.5-mm thickness, number of excitation [NEX] 4, scan time 8 minutes). Thirty slices were acquired to cover the brain from olfactory bulb to cervical spinal cord to screen for ventriculomegaly. T_2^*-weighted images were also acquired on every rat to examine the susceptibility vessel sign by multiple gradient echo (TR 60 ms, TE 3.18 ms, TE 3.25 ms, number of echo 14, FOV $3.5 \times 2.56 \times 1.4$ [cm]), matrix $175 \times 128 \times 70$, resolution 200 μm isotropic, NEX 2, scan time 17 minutes). 3D time-of-flight FLASH MRA was applied on 20 normal and 16 ventriculomegaly rats to examine the vascular abnormalities (TR 30 ms, TE 3.2 ms, FOV $1.4 \times 2.54 \times 1.8$ [cm], matrix $154 \times 280 \times 198$, voxel size 90 μm isotropic, NEX 3, scan time 30 minutes). Diffusion data were acquired on 38 normal and 24 ventriculomegaly rats (showing dilated ventricles on T_2-weighted images) to examine the tissue integrity of gray and white matter using 3D spin echo EPI (TR 700 ms, TE 37 ms, segment 4, 15 ms, δ 5 ms, b-value 0 and 800 s/mm^2 with 15 encoding directions, FOV 3.5

$\times$ 2.56 $\times$ 1.4 [cm], matrix 175 $\times$ 128 $\times$ 70, resolution 200 μm isotropic, NEX 1, total scan time 55 minutes).

MRI Data Processing and Analysis

The MRA examinations were reconstructed by Bruker's Imaging Processing toolbox to render the angiography of cerebral vasculature via maximum intensity projection. The T_2^* maps were created by fitting the magnitude images of each echo of the multiple gradient echo sequence to a single exponential on a pixel-by-pixel basis. Diffusion weighted images were corrected for B_0 susceptibility induced EPI distortion, eddy current distortions, and motion distortion with B-matrix reorientation using TORTOISE (17). After correction, the diffusion tensor was then calculated on voxel-by-voxel basis to derived DTI parameters, fractional anisotropy (FA), mean diffusivity (MD), axial diffusivity (AD), and radial diffusivity (RD), to inspect the tissue integrity according to the hypothesis that AD and RD could respectively reflect the extent of axon and myelin integrity, where FA and MD are sensitive to the increase of water content and overall microstructural architecture (18-22). Diffusion tensor tractography was performed using the fiber assignment by the continuous tracking algorithm implemented in the Diffusion Toolkit (23, 24), with an FA threshold of 0.3. The mean length of tracks within each of the regions of interest was determined with TrackVis (23). The DTI data were analyzed using ImageJ with regions of interest at the anterior commissure, corpus callosum, cerebral peduncle, external capsule, optic tract, striatum, and cortex. Hyperintense lesions or cysts were excluded in the regions of interest of DTI analysis to reflect the tissue integrity without bias. Data from 3 image slices were averaged to represent the DTI parameters for each anatomical region. Except for those processed by the aforementioned software, the imaging data were processed via in house MATLAB (MathWorks, Natick, MA) scripts.

Micro-CT and Immunohistochemistry Analysis

After the animals were killed, 3 abnormal rats with a diagnosis of large ventricle dilatation and abnormal vasculature by MRA were perfused with radiopaque Microfil® (Flow Tech, Carver, MA) at a 3:1 ratio of diluent to compound for subsequent micro-CT imaging of vasculature to scrutinize the suspected aneurysm and AVM nidus (25). Brain tissues were scanned using a SkyScan 1172 scanner (Bruker) with 0.4° angular increments, providing 900 views around 360°. Images were recorded, digitized, and transferred to a controlling computer. 3D volume images, which consisted of cubic voxels of 9.95 μm on-a-side, and the radiopacity of each voxel was represented by a 16-bit gray-scale value. CTVol v.2.2 (Bruker) were used to reconstruct the 3D CT images of the brain vasculatures.

Randomly selected rats with ventriculomegaly (n = 5) and normal rats (n = 5), based on T_2-weighted images, were killed with isoflurane and pentobarbital and perfused with 4% paraformaldehyde in phosphate buffered saline (PBS) for histologic analysis. The brain tissue was cryosectioned at 10 μm for IHC staining. Slides of sectioned tissue were washed with PBS, blocked in Superblock (ScyTek Laboratories, Logan, UT) for 10 minutes at room temperature and incubated in diluted primary antibody at 4°C overnight. The antibodies used were to: ionized calcium-binding adaptor molecule 1 (Iba1) (Wako, Richmond, VA) at 1/200 (for activated microglia), glial fibrillary acidic protein (GFAP) (Abcam, Cambridge,

MA) at 1/1500, (for astrocytes), (SMI31) (Covance, Princeton, NJ) at 1/1500, (for phosphorylated neurofilament H), hexaribonucleotide binding protein-3 (NeuN) (Abcam) at 1/1000, (for neurons), rat endothelial cell antigen (RECA1) (Abcam) at 1/750 (for vasculature), or myelin basic protein (MBP) (Abcam) at 1/500. The antibodies were diluted in 1x PBS, 0.3% Tween-20, and 1.0% bovine serum albumin. After 3 PBS + 0.3% Tween-20 washes, slides were incubated in secondary antibody as follows: for MBP and SMI31, goat F(ab') polyclonal secondary antibody to mouse IgG-H&L Dylight 594 (Abcam); for Iba-1 and GFAP, goat anti-rabbit F(ab') IgG- H&L Dylight 594 (Abcam) at a dilution of 1/200 in 1x PBS with 0.3% Tween-20 and 1.0% bovine serum albumin at room temperature for 1 hour. They were then rinsed 3 times in PBS + 0.3% Tween-20, dipped in dH2O, and mounted in ProLong Gold antifade with 4',6-diamidino-2-phenylindole (Invitrogen, Carlsbad, CA). Slides were visualized with an Aperio FL fluorescent microscope (Aperio, Vista, CA). Hematoxylin and eosin (H&E), and Luxol fast blue/ periodic acid Schiff stains were applied for brightfield microscopy to examine tissue morphology. Quantification of IHC staining was conducted by counting the numbers of positive staining in the 20X images using Matlab program CellC with manual confirmation (26).

Statistical Analysis

Statistical analysis was conducted using Prism software version 6.0c (GraphPad Software, Inc., La Jolla, CA, USA). Nonparametric Mann-Whitney U test was performed for statistical analysis to examine the difference between the normal and abnormal rats. p-value < 0.05 was considered indicative of a statistically significant difference. All data are reported as mean ± standard deviation (SD).

RESULTS

Pattern of Spontaneous Ventriculomegaly in Wistar Rats

From June 2012 to Dec. 2013, we observed that 43.2% of externally normal Wistar rats obtained from 2 different vendors displayed abnormalities in their CNS ventricular and vascular systems. Ventriculomegaly was associated with arachnoid cysts, white matter cysts and hyperintense CSF compartments by T_2-weighted images. Of the 162 rats evaluated with baseline MRI scans, 70 were abnormal (66 of 156 females and 4 of 6 males). Figure 2 demonstrates the patterns of mild ventriculomegaly observed in the rats in comparison to healthy controls by the anatomical T_2-weighted MRI. Compared to the normal brains (Fig. 2A), ventriculomegaly significantly changed the anatomy of the affected brains; ventriculomegaly (55/162), white matter cysts (22/162), enlarged BC (12/162), and various unidentified bright objects (13/162) were found in various locations (Fig. 2B). Quantification of the anomaly sizes normalized to the brain sections indicated the range of various sizes in the 8 anatomical locations (Fig. 2C). Three-dimensional volume rendering of the hyperintense region from a normal and a ventriculomegaly rat illustrated the enlarged ventricles and the arachnoid cysts in the posterior fossae (Fig. 2D). The histogram of ventriculomegaly rating scale implemented to evaluate abnormal patterns showed a bimodal population, i.e. a peak between score 0 and 1 and a positive skewed distribution from score 2 to 30 (Fig. 2E). 56.7% (92/162) of the rats had ventriculomegaly scores less than 2 (the

antimode) and were considered normal background. The compartment volumes of each anatomy normalized to the volumes of brain sections are listed in Table 1. Enlarged lateral ventricles (19.1%), 3rd ventricles (9.9%), and white matter cysts (13.6%) were the most frequent locations of ventriculomegaly. 8.0% of the animals had large aqueducts; 7.4% had enlarged BCs; 4.4% had an enlarged lateral recess of the 4th ventricle, 4.9% had enlarged 4th ventricles, and 3.7% had arachnoid cysts in the cerebellum. Aqueduct stenosis, a hallmark of many types of obstructive hydrocephalus or ventriculomegaly, was not observed in the rats.

Abnormal Vasculature, Astrogliosis, and Tissue Morphology Associated with Ventriculomegaly

Compared to the control brains (Fig. 3A-C), the T_2* maps revealed a paucity of susceptibility vessel sign in the cortex of the ventriculomegaly rats (Fig. 3E). A remarkable signal loss of healthy vessels, particularly in the venous system, was seen in the MRA of the ventriculomegaly rats (Fig. 3F). Among the 20 normal rats showing normal size of ventricles, 16 rats showed normal vasculatures, and 4 showed abnormal vasculatures by time-of-flight MRA. None of the 16 ventriculomegaly rats showed normal vasculature patterns on MRA. Vascular malformations were found near the confluence of sinus, including the transverse sinus, superior sagittal sinus and emissary vein (Fig. 3K-N).

Digital images of Microfil® cerebrovascular casting displayed many imaging irregularities of uncertain significance, similar to aneurysms or AVM niduses near the Circle of Willis in ventriculomegaly rats (Fig. 4A). Postmortem micro-CT images confirmed abnormal connections between veins and arteries in the potential AVM niduses in the ventriculomegaly rats (Fig. 4B); Luxol fast blue/periodic acid Schiff staining illustrated the morphology of the abnormal vessels in these areas (Fig. 4B inset). Smaller vessels with increased vessel density were seen in ventricles and at the BC indicating another abnormal pattern in the vasculature of the ventriculomegaly brains (Fig. 4C-F). Compared to the normal animals (Fig. 4G-I), there was increased astrogliosis surrounding the ventricles (Fig. 4J) and parenchymal blood vessels (Fig. 4K). Hypertrophy of astrocytic processes was also found in the cortex of the ventriculomegaly rats (Fig. 4L). A T_2-weighted image and corresponding H&E stain of a ventriculomegaly brain showed cysts in the cerebellum and brainstem (Fig. 5). An arachnoid cyst is shown on T_2-weighted image (Fig. 5A), where the H&E stain shows no tissue (Fig. 5B). Tissues near the cystic areas showed various degrees of necrosis (Fig. 5C-G), glial scarring (Fig. 5H-L), paucity of microvasculature (Fig. 5M-Q), and damage and loss of neurons (Fig. 5R-V).

Abnormal White Matter

DTI tractography of the ventriculomegaly brains revealed that the white matter tracts were abnormal and many were scarce; abnormalities involved the corpus callosum and tracts in thalamus and midbrain (Fig. 6A-D). In comparison to the normal rats, there were significantly lower FA (normal: 0.75 ± 0.04, ventriculomegaly: 0.67 ± 0.02, $p < 0.01$) and tract numbers (normal: 0.72 ± 0.15, ventriculomegaly: 0.53 ± 0.12, $p < 0.05$), and higher MD (normal: 0.85 ± 0.09, ventriculomegaly: 0.99 ± 0.11, $p < 0.01$, unit: $\mu m^2/ms$), AD (normal: 1.71 ± 0.14, ventriculomegaly: 1.90 ± 0.15, $p < 0.05$, unit: $\mu m^2/ms$), and RD (normal: 0.42 ± 0.10, ventriculomegaly: 0.54 ± 0.08, $p = 0.01$, unit: $\mu m^2/ms$) in the corpus

callosum of the ventriculomegaly rats. Cyst-like white matter lesion and enlarged ventricles greatly altered the white matter integrity and number of tracts (Fig. 6E-M). Table 2 lists the values of DTI parameters and the results of corresponding significance tests between the normal and ventriculomegaly rats, and values from both group of animals combined for statistical analysis. Significantly decreased FA and increased AD, RD, and MD were found in many major white matter tracts in the ventriculomegaly group (Table 2). White matter tract numbers were decreased in anterior commissure, corpus callosum, and optic nerve ($p < 0.05$), whereas the mean tract lengths were increased significantly ($p < 0.05$) in the cerebral peduncle. MD, AD, and RD were also increased in and cerebral cortex ($p < 0.05$). When data from the normal and ventriculomegaly rats were combined for statistical analysis, there were significantly different ADs in anterior commissure, cerebral peduncle, and optic nerve ($p < 0.05$) in comparison to the normal group.

Notable loss of SMI31 staining of neurofilaments was seen in the corpus callosum of the ventriculomegaly vs. the control rats (Fig. 7A, C). Axon counts (Fig. 8A) and SMI31 staining intensity (Fig. 8B) between gray and white matter were significantly lower ($p < 0.05$) in the ventriculomegaly rats. The thickness of corpus callosum was significantly thinner ($p < 0.01$) in the ventriculomegaly rats (0.47 ± 0.03 mm) in comparison to that of the normal rats (0.61 ± 0.04 mm). Astrogliosis was significantly increased in the cortex of the ventriculomegaly brain (Fig. 4L, 8C). No significant differences were found for myelin (Fig. 7B, D), astrocyte (Fig. 7E, H), microglia (Fig. 7F, I) or microvasculature (Fig. 7G, J) staining in the corpus callosum between the normal and ventriculomegaly rats.

DISCUSSION

Consistent animal models of neurological disorders are essential for basic investigations and the assessment of new diagnostic or therapeutic interventions. Wistar rats are commonly used in TBI studies. According to the PubMed database, in the 5,150 rat TBI research articles since 1990, nearly 22% (i.e., 1,151) of the studies reported their experimental results on Wistar rats. The current study documents the presence of mild spontaneous ventriculomegaly in more than 43% of the Wistar rats, along with the presence of possible AVMs or aneurysms, despite the fact that all of the rats had a normal external appearance. To our knowledge, this is the first report of this type of ventriculomegaly in Wistar rats by MRI, probably in part because there are no external manifestations of hydrocephalus/ ventriculomegaly in these young adult rats. Whenever possible, baseline scans are strongly suggested for Wistar rats prior to their use in studies of neurological disease, especially when testing diagnostic or therapeutic interventions.

Reviews of Hydrocephalus in Wistar Rats

Congenital spontaneous hydrocephalic LEW/Jms rats were discovered after repeated inbreeding of Wistar rats with hydrocephalus (4, 27). Inheritance of hydrocephalus in LEW/Jms rats is recessive, but affects more males than females, with an overall expression rate of 28% (4, 27). Hydrocephalus in the Wistar WIC-Hyd rat strain is inherited in a dominant fashion, with sex affecting the severity of hydrocephalus (3, 28). The overall prevalence of hydrocephalus in WIC-Hyd rats is 34.3% in males and 34.9% in females; 96%

of the hydrocephalic male rats are of the severe type; and 87% of the hydrocephalic female rats are of the moderate type (3). The ventricles, especially the lateral ventricles, are markedly dilated in the severely hydrocephalic brain, with a ruptured septum and a monoventricle. The severe hydrocephalic WIC-Hyd rats are externally abnormal, with a dome-shaped head, shortened nose, and slow growth. Moderately hydrocephalic (i.e. ventriculomegaly) WIC-Hyd rats show no clinical signs with respect to external appearance, activity, growth or behavior.

Patterns of Ventriculomegaly in Wistar Rats

In comparison to the ventricular enlargement associated with induced hydrocephalus models and genetic models wherein the cerebrum can be reduced to a paper-thin thickness, the hydrocephalus pattern observed in the current study is much less severe, i.e. characterized by mildly dilated ventricles, scattered intracranial arachnoid cysts (in both gray and white matter) and more rarely observed necrotic paraflocculi and cerebellum. Rats with these mild hydrocephalus patterns showed no evidence of abnormalities in skull size in young adulthood. The ventriculomegaly Wistar rats were externally asymptomatic, and by imaging displayed a communicating type of hydrocephalus, i.e. mild ventriculomegaly with no evidence of aqueduct stenosis, and various types of cysts or T_2-weighted hyperintense lesions (Table 1). The pattern was characteristic of a spontaneous origin, i.e. unlikely to have been caused by post-natal obstructive, infectious, inflammatory, traumatic, or hemorrhagic events (Figs. 4, 5, 7). The DTI tractography clearly showed adaptation of white matter tracts to structural changes associated with ventriculomegaly or cystic lesions (Fig. 6). The measurement of corpus callosum thickness substantiates the DTI tractography results, i.e. the ventriculomegaly rats had thinner corpus callosum vs. the normal rats (Fig. 7).

Abnormal SMI31 staining intensity of neurofilament was also seen in the corpus callosum of ventriculomegaly rats while SMI31 staining in gray matter was normal (Fig. 7A, C). The mechanism underlying the loss of SMI31 in the corpus callosum is unclear. Ventriculomegaly may be responsible for causing injury to periventricular axons, microvessels, and delayed demyelination (29). Extensive astrogliosis was observed not only near ventricles and large vessels of the ventriculomegaly rats but also in the cerebral cortex. This was likely associated with prolonged neuroinflammation, impaired cerebral perfusion, altered blood-brain barrier function, inhibited repair of damaged neural tissue, impeded neuronal plasticity, and altered intracranial compliance (30-36). We postulate that the ventriculomegaly rats might have developmental aberrations in the blood-brain barrier system due to defective tight junctions and increased cranial pressure. Necrotic tissue, marked cell loss, axonal loss, glial scarring and paucity of microvessels were adjacent to the arachnoid cysts (Fig. 5), which may have resulted from ischemic events or hypoxia when the defective vasculature could not provide sufficient blood supply. The local vasculature malformation might have caused ischemic cell death, and some of the intracranial CSF cysts were likely the consequence of such ischemic events and tissue clearance.

Imaging of CNS Abnormalities

Ventriculomegaly coexisting with intracranial cysts or hyperintense lesions on T_2-weighted images occurs in humans (37-39). The cystic cavity may be formed by congenital duplication or splitting of the arachnoid membrane or glia cells. Arachnoid cysts may be a compartmentalized form of a re-absorptive ventriculomegaly, probably harboring a latent aberration of CSF circulation (40)

The DTI results showed a decrease in FA and an increase in AD and RD in many white matter tracts, suggesting that white matter integrity is different between the normal and ventriculomegaly rats (Table 2). Except for the tract lengths, all of the DTI indices measured in the corpus callosum were significantly different between the normal and ventriculomegaly rats ($p < 0.05$). These results suggest that increased water content in the ventriculomegaly rats alters white matter structure, and potentially DTI measurements. This observation has direct relevance to a current hypothesis for interpretation of DTI results: increases of FA and AD indicate an increase in axonal integrity, while an increase in RD reflects demyelination (21, 41-44). The increased water content in the ventriculomegaly Wistar rats results in decreases in FA and increases in both AD and RD, with changes in neurofilament quality (as assessed by SMI31 immunostaining), but no associated changes in myelin (45, 46). The excessive astrogliosis may also contribute to the increase of AD and FA in the cortex of ventriculomegaly rats (19). If ventriculomegaly rats are included in DTI experiments, as shown in Table 2, the results could deliver the false interpretation of a pseudo-increase of axon integrity and a pseudo-decrease of myelin integrity purely based on characteristics intrinsic to these rats (18). These discrepancies also indicate the importance of histopathology in assessing the relationship between in vivo DTI 'biomarkers' and underlying mechanisms.

The whole brain MRA revealed a contrast loss of healthy vasculature in all of the ventriculomegaly rats and a small portion (4 out of 20) of non-ventriculomegaly rats, particularly in the venous system (Fig. 3F, K-N). The micro-CT results revealed abnormalities in the cerebral vascular system of the examined subset of these ventriculomegaly rats, suggesting either AVMs and/or aneurysms (Fig. 4B). RECA1 staining disclosed the excessive branching of vessels, although whether the changes in the vasculature contribute to the observed ventriculomegaly, are a compensatory mechanism in response to it, or are merely correlated but not directly associated, is not currently known (Fig. 4C-F). The lack of susceptibility vessel signal on T_2*-weighted images indicate either reduced amounts of blood or slowed cerebral blood flow, possibly resulting in increased CSF volume or interstitial pressure (47-51). If increased pressure at the arachnoid granulations obstructs the passive CSF flow into the sinuses, CSF might accumulate in the closed compartments. The presence of AVMs and aberrant vasculature near the confluence of sinuses might also affect the reabsorption of CSF into the systemic circulation, contributing to the formation of ventriculomegaly.

Limitations of this Study

The abnormalities observed in this study arose as incidental findings in our investigations of TBI primarily in female rats that were used for their smaller sizes to fit in our imaging setup.

We examined a small sample of male rats from the same vendors to determine whether comparable abnormalities were observed in a similar percentage of male rats. The similar percentages we observed in our larger cohort of female rats and in the smaller cohort of male rats indicate that the abnormalities reported herein occur irrespective of biological sex. Whether there are more subtle sex-specific effects is beyond the scope of this report. Meanwhile, noninvasive MRI was the main tool for screening the appearance and factors of ventriculomegaly. As most of the imaging study with limited resources and time, only a small subset of rats were performed Micro-CT and IHC analyses to verify the MRI findings. Increasing sample size and further analyses would be required for detailed pathological and genetic analyses of the ventriculomegaly Wistar rats. It is noted that the high prevalence of ventriculomegaly was observed mainly due to our strict criteria of screening ventriculomegaly-associated anomalies by high-resolution MRI. The results may not be comparable to reports in the literature using lower screening resolution histological examination.

While there is debate about whether rodent models accurately reflect human disease, rats are by far still among the most commonly used species to model neurological diseases (52). When much attention has been given to the generation of disease models, the baseline characteristics of the animals used have typically been assumed to be normal in the absence of external behavioral or physical signs. The inadvertent inclusion of ventriculomegaly Wistar rats in neurological studies may contribute variability to experiments that lead to unforeseen bias in studies of low sample size (53). Beyond the implications that these ventriculomegaly rats may have for interpretation of experimental results, this newly documented form of ventriculomegaly may be importance as an animal model to study hydrocephalus/ventriculomegaly in association with cyst formation and/or vascular malformations.

Summary

We report the presence of spontaneous mild ventriculomegaly in Wistar rats in approximately 43% of animals. Multiple abnormalities, including AVM, aneurysms, ventriculomegaly, intracranial cysts, white matter injury, tissue necrosis and excessive astrogliosis, were associated with ventriculomegaly. The DTI parameters correlated with various abnormalities secondary to increased water content but did not reliably reflect the white matter integrity in ventriculomegaly animals. These anomalies associated with ventriculomegaly in the Wistar rats introduce variability in models when these animals are included in experiments. Baseline scans are strongly suggested to prevent the accidental use of these ventriculomegaly animals, or increased sample sizes and random allocation of animals to treatment groups, in the study of neurological disease, particularly when testing therapeutic interventions.

Acknowledgments

REFERENCES

1. Franklin JB, Brent RL. The effect of uterine vascular clamping on the development of rat embryos three to fourteen days old. J Morphol. 1964; 115:273–90. [PubMed: 14214410]

2. Kohn DF, Chinookoswong N, Chou SM. A new model of congenital hydrocephalus in the rat. Acta Neuropathol. 1981; 54:211–8. [PubMed: 7257730]

3. Koto M, Miwa M, Shimizu A, et al. Inherited hydrocephalus in Csk: Wistar-Imamichi rats; Hyd strain: a new disease model for hydrocephalus. Jikken Dobutsu. 1987; 36:157–62. [PubMed: 2956117]

4. Sasaki S, Goto H, Nagano H, et al. Congenital hydrocephalus revealed in the inbred rat, LEW/Jms. Neurosurgery. 1983; 13:548–54. [PubMed: 6606138]

5. Jones HC, Totten CF, Mayorga DA, et al. Genetic loci for ventricular dilatation in the LEW/Jms rat with fetal-onset hydrocephalus are influenced by gender and genetic background. Cerebrospinal Fluid Res. 2005; 2:2. [PubMed: 15953386]

6. Mulla MSA, Goyal VK, Jana S, et al. Spontaneous congenital hydrocephalus in Sprague Dawley rat. Scand J Lab Animal Sci. 2012; 39:65–8.

7. Van Eden CG, Mullink JW. Internal hydrocephalus, optic nerve aplasia, and microphthalmia in CPB-WE (Wezob) and Cpb:WU (Wistar) rats. Lab Anim. 1986; 20:257–65. [PubMed: 3795865]

8. McAllister JP 2nd. Pathophysiology of congenital and neonatal hydrocephalus. Semin Fetal Neonatal Med. 2012; 17:285–94. [PubMed: 22800608]

9. Brodbelt A, Stoodley M. CSF pathways: a review. Br J Neurosurg. 2007; 21:510–20. [PubMed: 17922324]

10. Diringer MN, Edwards DF, Zazulia AR. Hydrocephalus: a previously unrecognized predictor of poor outcome from supratentorial intracerebral hemorrhage. Stroke. 1998; 29:1352–7. [PubMed: 9660386]

11. Kohn DF, Kirk BE, Chou SM. Mycoplasma-induced hydrocephalus in rats and hamsters. Infect Immun. 1977; 16:680–9. [PubMed: 558963]

12. Jones HC, Bucknall RM. Inherited prenatal hydrocephalus in the H-Tx rat: a morphological study. Neuropathol Appl Neurobiol. 1988; 14:263–74. [PubMed: 3221976]

13. Ohmiya M, Fukumitsu H, Nitta A, et al. Administration of FGF-2 to embryonic mouse brain induces hydrocephalic brain morphology and aberrant differentiation of neurons in the postnatal cerebral cortex. J Neurosci Res. 2001; 65:228–35. [PubMed: 11494357]

14. Miyan JA, Mashayekhi F, Bannister CM. Developmental abnormalities in early-onset hydrocephalus: clues to signalling. Symp Soc Exp Biol. 2001:91–106. [PubMed: 12063851]

15. Fukumitsu H, Ohmiya M, Nitta A, et al. Aberrant expression of neurotrophic factors in the ventricular progenitor cells of infant congenitally hydrocephalic rats. Childs Nerv Syst. 2000; 16:516–21. [PubMed: 11007504]

16. Zhang J, Williams MA, Rigamonti D. Genetics of human hydrocephalus. J Neurol. 2006; 253:1255–66. [PubMed: 16773266]

17. Pierpaoli, C.; Walker, L.; Irfanoglu, MO., et al. TORTOISE: an integrated software package for processing of diffusion MRI data; ISMRM 18th annual meeting; Sweden. 2010; p. #1597

18. Tu TW, Frank JA. Assessing white matter integrity in experimental spinal cord injury using diffusion tensor imaging. J Neurosci and Neuroengineering. 2013; 2:415–30.

19. Budde MD, Xie M, Cross AH, et al. Axial diffusivity is the primary correlate of axonal injury in the experimental autoimmune encephalomyelitis spinal cord: a quantitative pixelwise analysis. J Neurosci. 2009; 29:2805–13. [PubMed: 19261876]

20. Song SK, Sun SW, Ramsbottom MJ, et al. Dysmyelination revealed through MRI as increased radial (but unchanged axial) diffusion of water. Neuroimage. 2002; 17:1429–36. [PubMed: 12414282]

21. Song SK, Sun SW, Ju WK, et al. Diffusion tensor imaging detects and differentiates axon and myelin degeneration in mouse optic nerve after retinal ischemia. Neuroimage. 2003; 20:1714–22. [PubMed: 14642481]

22. Tu TW, Budde MD, Xie M, et al. Phase-aligned multiple spin-echo averaging: a simple way to improve signal-to-noise ratio of in vivo mouse spinal cord diffusion tensor image. Magn Reson Imaging. Aug 1.2014 pii: S0730-725X(14)00207-0. doi: 10.1016/j.mri.2014.07.004. [Epub ahead of print].

23. Wang R, Benner T, Sorensen AG, et al. Diffusion Toolkit: A Software Package for Diffusion Imaging Data Processing and Tractography. Proceeding of International Society of Magnetic Resonance in Medicine. 2007; 15:3720.

24. Johnson GA, Calabrese E, Badea A, et al. A multidimensional magnetic resonance histology atlas of the Wistar rat brain. Neuroimage. 2012; 62:1848–56. [PubMed: 22634863]

25. Walker EJ, Shen F, Young WL, et al. Cerebrovascular casting of the adult mouse for 3D imaging and morphological analysis. J Vis Exp. Nov 30.2011 :57. doi: 10.3791/2958 2958.

26. Selinummi J, Seppala J, Yli-Harja O, et al. Software for quantification of labeled bacteria from digital microscope images by automated image analysis. Biotechniques. 2005; 39:859–63. [PubMed: 16382904]

27. Otsubo Y, Ito H, Shibuya T. Intracerebral monoamine concentration after ventriculoperitoneal shunting in the congenital hydrocephalus rat. Neurol Med Chir (Tokyo). 1997; 37:669–76. [PubMed: 9330530]

28. Shimizu A, Koto M. Ultrastructure and movement of the ependymal and tracheal cilia in congenitally hydrocephalic WIC-Hyd rats. Childs Nerv Syst. 1992; 8:25–32. [PubMed: 1576603]

29. Jain-Ghai S, Mishra N, Hahn C, et al. Fetal onset ventriculomegaly and subependymal cysts in a pyridoxine dependent epilepsy patient. Pediatrics. 2014; 133:e1092–6. [PubMed: 24664088]

30. Miller JM, McAllister JP 2nd. Reduction of astrogliosis and microgliosis by cerebrospinal fluid shunting in experimental hydrocephalus. Cerebrospinal Fluid Res. 2007; 4:5. [PubMed: 17555588]

31. Eskandari R, Harris CA, McAllister JP 2nd. Reactive astrocytosis in feline neonatal hydrocephalus: acute, chronic, and shunt-induced changes. Childs Nerv Syst. 2011; 27:2067–76. [PubMed: 21847645]

32. Yoshida Y, Koya G, Tamayama K, et al. Development of GFAP-positive cells and reactive changes associated with cystic lesions in HTX rat brain. Neurol Med Chir (Tokyo). 1990; 30:445–50. [PubMed: 1701853]

33. Khan OH, Enno TL, Del Bigio MR. Brain damage in neonatal rats following kaolin induction of hydrocephalus. Exp Neurol. 2006; 200:311–20. [PubMed: 16624304]

34. Deren KE, Packer M, Forsyth J, et al. Reactive astrocytosis, microgliosis and inflammation in rats with neonatal hydrocephalus. Exp Neurol. 2010; 226:110–9. [PubMed: 20713048]

35. Del Bigio MR. Pathophysiologic consequences of hydrocephalus. Neurosurg Clin N Am. 2001; 12:639–49. vii Review. [PubMed: 11524286]

36. McAllister JP 2nd, Miller JM. Minocycline inhibits glial proliferation in the H-Tx rat model of congenital hydrocephalus. Cerebrospinal Fluid Res. 2010; 7:7. [PubMed: 20507614]

37. Levy ML, Meltzer HS, Hughes S, et al. Hydrocephalus in children with middle fossa arachnoid cysts. J Neurosurg. 2004; 101:25–31. [PubMed: 16206968]

38. Itakura T, Takifuji K, Ozaki F, et al. Cystic arteriovenous malformation. A case report. Acta Neurochir (Wien). 1989; 96:154–8. [PubMed: 2711901]

39. Sabharwal P, Maiti T, Konar S, et al. Arteriovenous malformation associated with cyst in a child: Case report and review of literature. J Pediatr Neurosci. 2013; 8:126–8. [PubMed: 24082931]

40. Sival DA, Guerra M, den Dunnen WF, et al. Neuroependymal denudation is in progress in full-term human foetal spina bifida aperta. Brain Pathol. 2011; 21:163–79. [PubMed: 21269337]

41. Xie M, Tobin JE, Budde MD, et al. Rostrocaudal analysis of corpus callosum demyelination and axon damage across disease stages refines diffusion tensor imaging correlations with pathological features. J Neuropathol Exp Neurol. 2010; 69:704–16. [PubMed: 20535036]

42. Kraus MF, Susmaras T, Caughlin BP, et al. White matter integrity and cognition in chronic traumatic brain injury: a diffusion tensor imaging study. Brain. 2007; 130:2508–19. [PubMed: 17872928]

43. Ding GL, Chopp M, Poulsen DJ, et al. MRI of neuronal recovery after low-dose methamphetamine treatment of traumatic brain injury in rats. PLoS One. 2013; 8:e61241. [PubMed: 23637800]

44. Tu TW, Kim JH, Wang J, et al. Full tensor diffusion imaging is not required to assess the white-matter integrity in mouse contusion spinal cord injury. J Neurotrauma. 2010; 27:253–62. [PubMed: 19715399]

45. Tu TW, Kim JH, Yin FQ, et al. The impact of myelination on axon sparing and locomotor function recovery in spinal cord injury assessed using diffusion tensor imaging. NMR Biomed. 2013; 26:1484–95. [PubMed: 23775778]

46. Wang Y, Wang Q, Haldar JP, et al. Quantification of increased cellularity during inflammatory demyelination. Brain. 2011; 134:3590–601. [PubMed: 22171354]

47. Bragin DE, Bush RC, Muller WS, et al. High intracranial pressure effects on cerebral cortical microvascular flow in rats. J Neurotrauma. 2011; 28:775–85. [PubMed: 21395499]

48. Myers RR, Mizisin AP, Powell HC, et al. Reduced nerve blood flow in hexachlorophene neuropathy: relationship to elevated endoneurial fluid pressure. J Neuropathol Exp Neurol. 1982; 41:391–9. [PubMed: 6283035]

49. Yang GY, Betz AL, Chenevert TL, et al. Experimental intracerebral hemorrhage: relationship between brain edema, blood flow, and blood-brain barrier permeability in rats. J Neurosurg. 1994; 81:93–102. [PubMed: 8207532]

50. Grubb RL Jr. Raichle ME, Phelps ME, et al. Effects of increased intracranial pressure on cerebral blood volume, blood flow, and oxygen utilization in monkeys. J Neurosurg. 1975; 43:385–98. [PubMed: 808593]

51. Alperin N, Hushek SG, Lee SH, et al. MRI study of cerebral blood flow and CSF flow dynamics in an upright posture: the effect of posture on the intracranial compliance and pressure. Acta Neurochir Suppl. 2005; 95:177–81. [PubMed: 16463846]

52. Couzin-Frankel J. When mice mislead. Science. 2013; 342:922–3. 5. [PubMed: 24264972]

53. Turtzo LC, Budde MD, Gold EM, et al. The evolution of traumatic brain injury in a rat focal contusion model. NMR Biomed. 2012
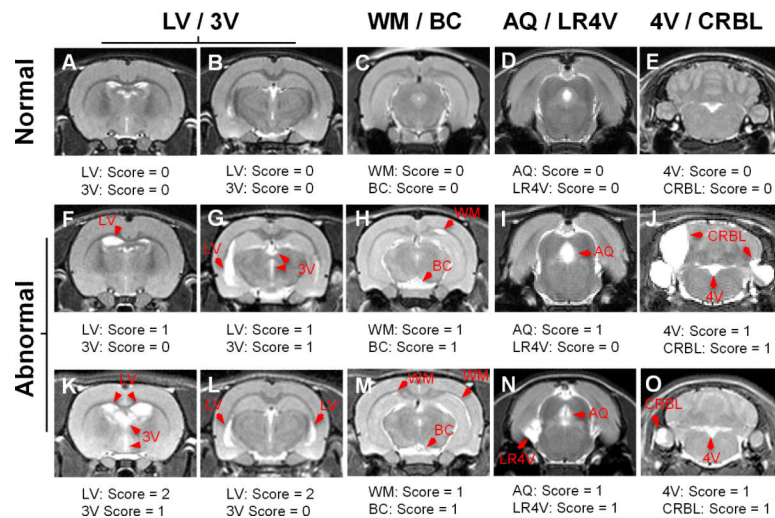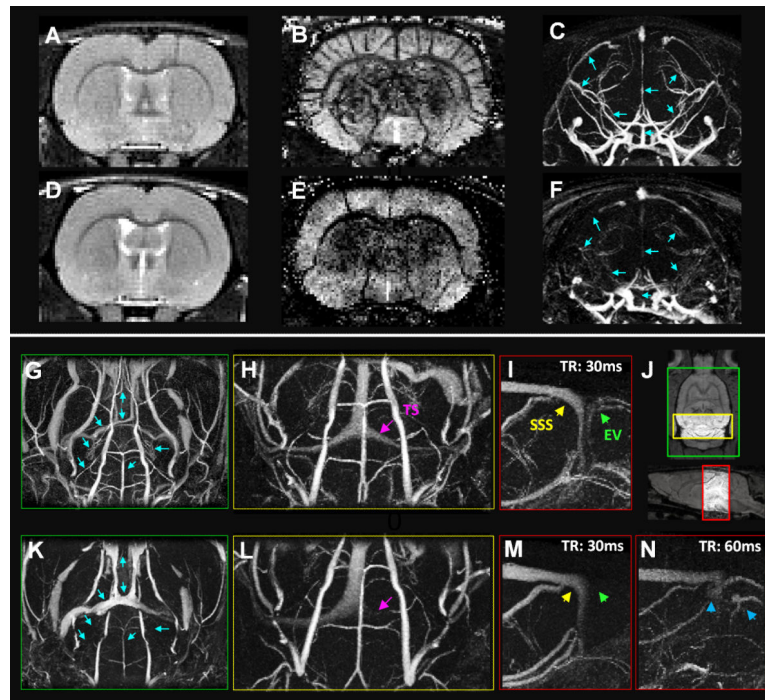
Figure 1.
CSF compartment scoring basis for Wistar rats. (**A-O**) Ventriculomegaly patterns were rated at 8 anatomical locations: lateral ventricles (LV), 3rd ventricle (3V), 4th ventricle (4V), aqueduct (AQ), lateral recess of 4th ventricle (LR4V), white matter (WM), basal cisterns (BC), and cerebellum (CRBL) based on 30 consecutive T$_2$-weighted images covering from olfactory bulb to cerebellum. The lateral ventricles were rated 0 for normal appearance (**A**), 1 for unilateral anomalous appearance (arrows in **F, G**), or 2 for bilateral abnormal appearance (arrows in **K, L**). All other anatomical locations were scored 0 for normal (**A-E**) or 1 for abnormal (arrows in **F-O**) appearance. Scores from 8 anatomical locations were then summed for each animal for its final score.
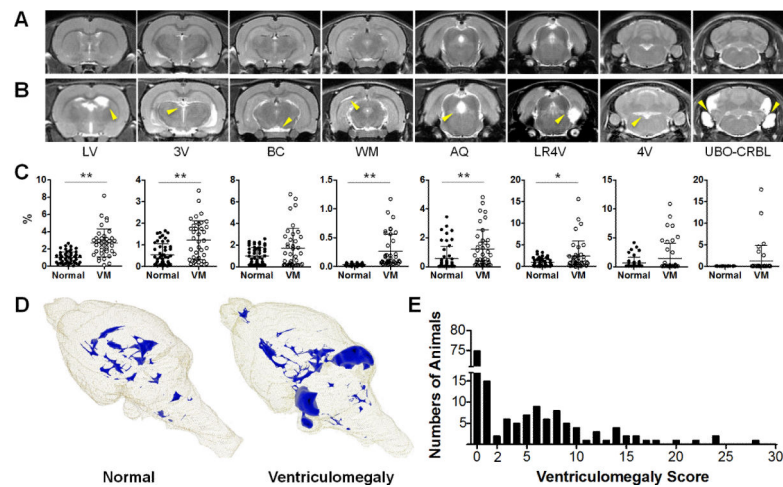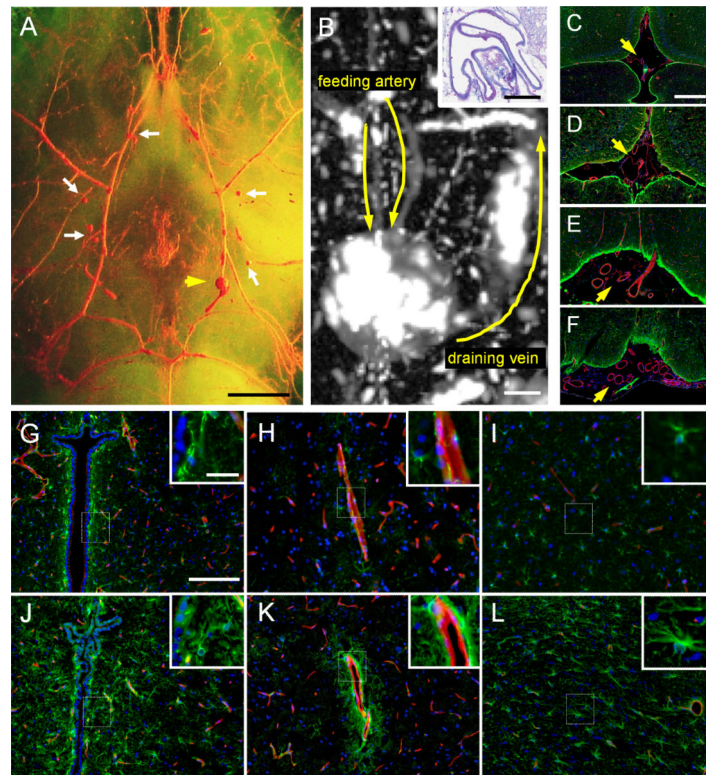
Figure 2.
Spontaneous ventriculomegaly and normal rat brains in anatomical T_2-weighted images. (**A, B**) Compared to the rats with normal ventricles and structures in series of T_2-weighted images (**A**), asymmetric ventriculomegaly and unidentified bright object bright objects (UBO) were found in the ventriculomegaly rats (**B**). Arrows indicate the enlarged ventricles, BC, and UBO in various locations. (**C**) Quantification of the normalized ventricle sizes indicates the distribution of the anomaly in ventriculomegaly rats. (**D**) Three-dimensional volume rendering of the ventricles from a normal and an abnormal rat shows the ventriculomegaly and cysts in ventricles and cerebellum. (**E**) Scores from 162 Wistar rats demonstrate a bimodal distribution with a peak at score 0 and a positive skewed distribution from 2 to 30 in which the cut-off score is 2 for showing ventriculomegaly. Bars in each panel in **C** are plotted as mean ± SD, * $p < 0.05$, ** $p < 0.01$. LV, left ventricle; 3V, 3rd ventricle; BC, basal cisterns; UBO, unidentified bright object; WM, white matter; AQ, aqueduct; LR4V, lateral recess of the 4th ventricle; 4V, 4th ventricle; CRBL, cerebellum; VM, ventriculomegaly.
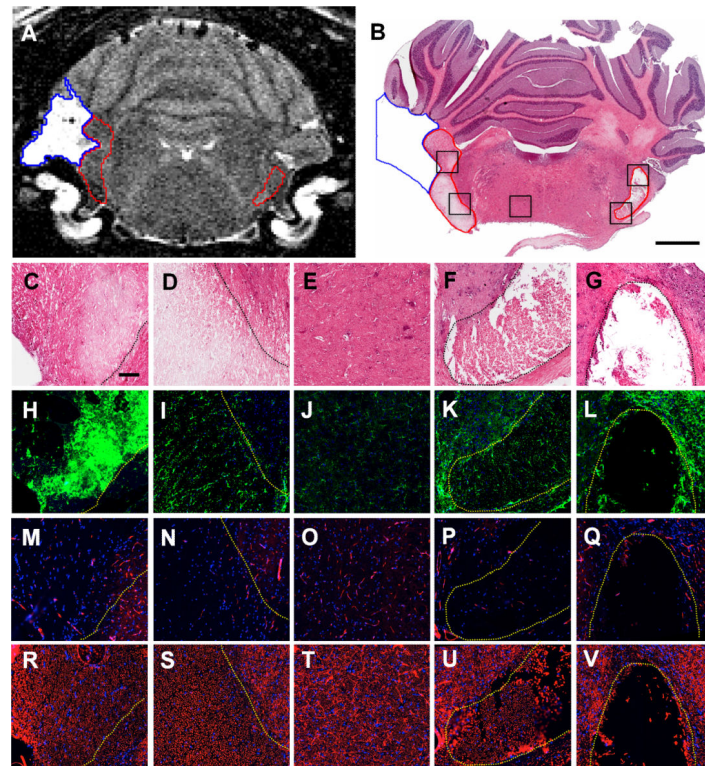
Figure 3.
(**A-N**) Representative anatomical T_2-weighted images (A, D, J), T_2* map (**B, E**), and magnetic resonance angiography (MRA) (**C, F, G-I, K-N**) of a normal and a ventriculomegaly rat. Compared to normal rats (**A-C, G-I**), the ventriculomegaly rats show abnormal vasculature in the brains (**E, F, K-N**). The ventriculomegaly brain exhibits marked loss of T_2* susceptibility vessel sign in the T_2* map (**E**). The coronal views of MRA images (**C, F**) also show a notable signal loss of the vessels (arrows), especially in the venous system in the ventriculomegaly rats (**F**). The anatomical image (**J**) illustrates the locations for the MRA acquisitions (green for **G, K**; yellow for **H, L**; red for **I, M, N**). A remarkable number of imaging irregularities of uncertain significance (arrows), possible aneurysms and arteriovenous/vascular malformations, are seen in the MRA of the ventriculomegaly rat brain (**K, L**) in contrast to the healthy vessels in normal rats (**G, H**). Transverse sinus (TS, pink) is less apparent in the MRA of the ventriculomegaly rat (**L**). The superior sagittal sinus (SSS, yellow) and emissary vein (EV, green) are clearly seen in the normal rat using TR = 30 ms in MRA (**I**). EV is not observed in the ventriculomegaly rat using the same TR (**M**). Tortuosity of the EVs appears (blue arrows) when TR was increased to 60 ms, suggesting slower blood flow in these vessels (N).
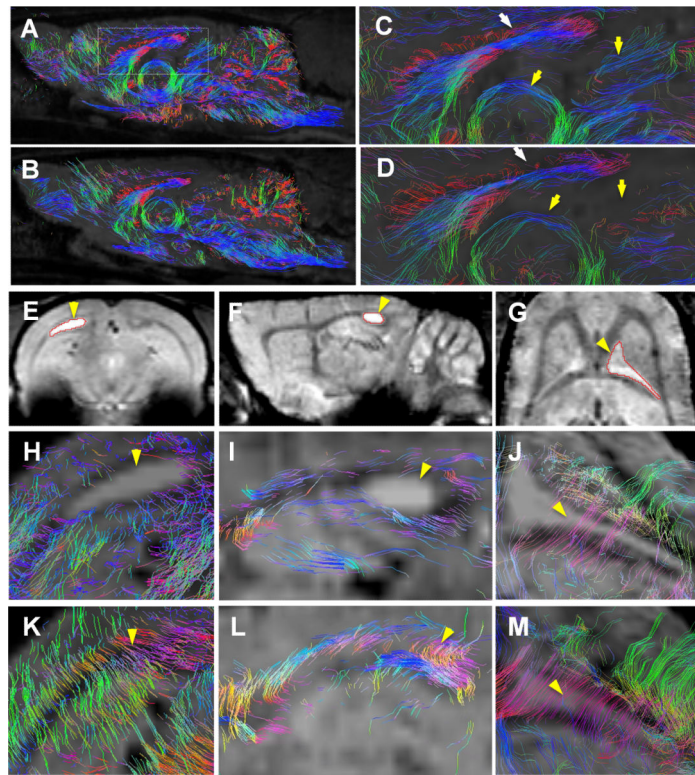
Figure 4.
Arteriovenous malformation (AVM) nidus, abnormal vessel branching, and excessive astrogliosis in ventriculomegaly rat brains identify by micro-CT and optical microscopy. (**A**) Photograph of a Microfil® perfused ventriculomegaly brain after clarification shows many AVM niduses (arrow and arrowheads) near the Circle of Willis. (**B**) Micro-CT image demonstrates an abnormal tangle of blood vessels in an AVM nidus indicated by the yellow arrowhead in (**A**). Connection of the feeding artery and the AVM nidus draining into a dilated vein (arrows), which is a hallmark of AVM. Inset in the upper right corner is a Luxol fast blue/ PAS stain illustrating the abnormal vessel morphology. (**C-L**) Immunohistochemistry for glial fibrillary acidic protein (GFAP, green), rat endothelial cell antigen (RECA1) (red) and 4',6-diamidino-2-phenylindole (DAPI) (blue) demonstrate the astrocytes, blood vessel and nuclei, respectively, in normal (**C, E, G-I**) and ventriculomegaly (**D, F, J-**L) rats. In the ventriculomegaly rat there is abnormal vessel branching in the ventricles (**D**) and basal cistern (**F**). There is marked astrogliosis in the ventriculomegaly rat brain surrounding the ventricle (**J**) and blood vessels (**K**). Hypertrophy of astrocytic processes is also seen in the cortex of the ventriculomegaly rat brain (**L**). Scale bar: **A**, 2 mm; **B-F**: 200 μm; **G-L**, 100 μm [25 μm in magnified images in **G-L**).
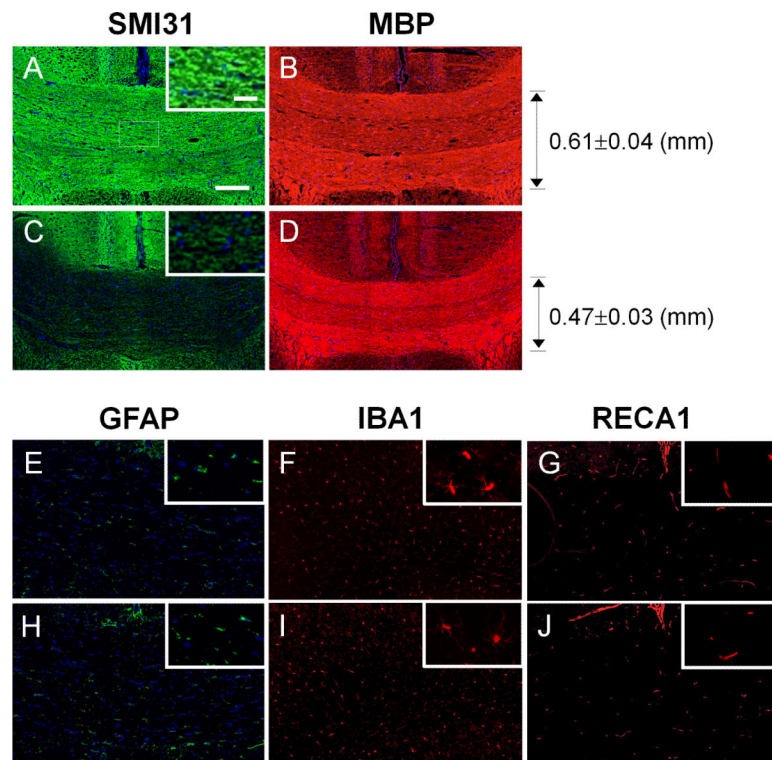
Figure 5.
Morphological patterns of necrosis adjacent to arachnoid cysts. (**A-V**) T_2-weighted image (**A**), hematoxylin and eosin (H&E) (**B-G**), glial fibrillary acidic protein (GFAP) (**H-L**), RECA1 (**M-Q**), and NeuN (**R-V**) immunohistochemical staining of a ventriculomegaly brains. An arachnoid cyst (blue region of interest [ROI] in **A** and **B**), with contrast close to CSF in the T_2-weighted image, is found in the paraflocculus. Another cyst-like lesion appears only in the H&E stain, where the T_2-weighted image shows normal contrast (red ROI in **A** and **B**). Compared to the normal tissue (**E, J, O, T**), the arachnoid cyst space lacks normal tissue structures in the H&E stain (**C, D, F, G**) and is surrounded by glial scarring (**H, I, K, L**). The necrotic tissue is largely scarce in microvasculature in the RECA1 immunostaining (**M, N, P, Q**) and shows damage and loss of neurons in brainstem (**R, S, U, V**). The magnified images (**C-V**) in each column were taken from the corresponding locations indicated by the squares in (**B**) (from left to right). Dashed lines highlight the borders of arachnoid cyst or cyst-like lesion. Scale bars: **B**, 2 mm; **C-V**, 100 μm.

Figure 6.
(**A-M**) Diffusion tensor imaging (DTI) tractography from normal (**A, C, K-M**) and ventriculomegaly (**B, D, H-J**) rats. The magnified images (**C, D**), taken from the region indicated in (**A**), show white matter rarefaction in the corpus callosum, mammillothalamic and habenulopeduncular tract in the ventriculomegaly rat (**B, D**) vs. the normal rat (**A, C**). White matter tracts of the ventriculomegaly rat brains (**H-J**) were affected by the cyst-like white matter lesions (**E, F**) and ventriculomegaly (**G**). The normal rats show abundant healthy white matter tracts in the same locations (**K-M**). These results indicate that the increased water content in the ventriculomegaly rat alters the DTI measurements and the white matter structure.

Figure 7.

Representative immunohistochemistry for phosphorylated neurofilament (SMI31) (**A, C**), myelin basic protein (MBP) (**B, D**), glial fibrillary acidic protein (GFAP) (**E, H**), ionized calcium-binding adaptor molecule 1 (IBA1) (**F, I**) and rat endothelial cell antigen (RECA1) (**G, J**) in the corpus callosum of normal (**A, B, E-G**) and ventriculomegaly (**C, D, H-J**) rats. The increased water content was associated with the loss of SMI31 staining in the corpus callosum of ventriculomegaly rats (**A** vs. **C**). No significant difference is found in the MBP, GFAP, Iba1, and RECA1 immunostaining between the normal and hydrocephalic rats. Ventriculomegaly rats have significantly thinner corpus callosum (0.47 ± 0.03 mm) vs. the normal rats (0.61 ± 0.04 mm) (**B, D**). The high-magnification images in **A-J** were taken from the region indicated in **A**. Scale bars: **A-J**, 250 μm (30 μm in magnified insets in **A-J**).
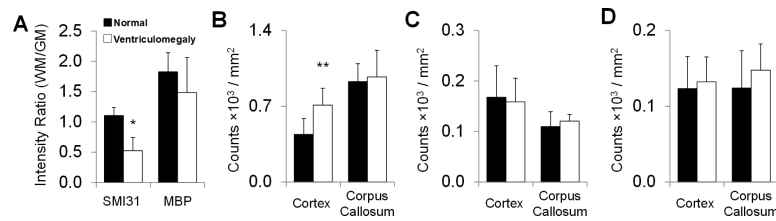
Figure 8.
Quantification of immunohistochemistry for phosphorylated neurofilament (SMI31) and myelin basic protein (MBP) (**A**), glial fibrillary acidic protein (GFAP) (**B**), ionized calcium-binding adaptor 1 (Iba1) (**C**), and rat endothelial cell antigen (RECA1) (**D**) in the cortex and corpus callosum of normal and ventriculomegaly rats. (**A**) The SMI31 stain intensity ratio between white and gray matter was significantly different between normal and ventriculomegaly rats ($p < 0.05$). MBP ratios were not different. (**B**) GFAP counts were significantly greater in the cortex (see Fig. 4I, L), but not in the corpus callosum in ventriculomegaly vs. normal rats. (**C, D**) There were no significant difference in Iba1 (**C**) or RECA1 (**D**) staining in both cortex and corpus callosum between normal and ventriculomegaly rats. * $p < 0.05$, ** $p < 0.01$.

Table 1

Compartment Volume of Each Anatomy Normalized to the Volume of the Brain Section for the Normal and Ventriculomegaly Rats

Anatomy	Compartment Size (%)		Number of Abnormal Rats
	Normal	Ventriculomegaly	
Lateral Ventricle	0.98 ± 0.66	2.57 ± 1.37 **	31 (19.1%)
3rd Ventricle	0.56 ± 0.50	1.16 ± 0.83 **	16 (9.9%)
Basal Cistern	1.01 ± 0.79	1.55 ± 1.68	12 (7.4%)
White Matter Cyst	0.03 ± 0.02	0.24 ± 0.26 **	22 (13.6%)
Aqueduct	0.51 ± 0.76	1.17 ± 1.31 **	13 (8.0%)
Lateral Recess of 4th Ventricle	0.99 ± 0.88	2.11 ± 2.68 *	7 (4.3%)
4th Ventricle	0.59 ± 0.96	1.30 ± 2.52	8 (4.9%)
UBO-Cerebellum	0.16 ± 0.02	1.04 ± 3.10	6 (3.7%)

Data are reported as mean percentages ± SD

UBO, unidentified bright objects.

*
$p < 0.05$

**
$p < 0.01$.

Table 2

Diffusion Tensor Imaging Parameters for Normal, Ventriculomegaly and Combined Rat Groups

Anatomy	Group	FA	MD (μm^2/ms)	$\lambda_{\parallel}$ (μm^2/ms)	$\lambda_{\perp}$ (μm^2/ms)	Tract Number (Counts/Voxel)	Mean Tract Length (mm)
Anterior Commissure	Normal	0.79 ± 0.04	0.79 ± 0.08	1.75 ± 0.16	0.34 ± 0.07	0.31 ± 0.04	2.54 ± 0.73
	Ventriculomegaly	0.77 ± 0.04	0.90 ± 0.07**	1.98 ± 0.19**	0.36 ± 0.05	0.24 ± 0.03**	2.77 ± 0.85
	Combined	0.78 ± 0.04	0.84 ± 0.10	1.85 ± 0.21*	0.34 ± 0.06	0.28 ± 0.05	2.57 ± 0.79
Corpus Callosum	Normal	0.75 ± 0.04	0.85 ± 0.09	1.71 ± 0.14	0.42 ± 0.10	0.72 ± 0.15	1.99 ± 0.74
	Ventriculomegaly	0.67 ± 0.02**	0.99 ± 0.11**	1.90 ± 0.15*	0.54 ± 0.08**	0.53 ± 0.12*	1.95 ± 0.87
	Combined	0.71 ± 0.04	0.92 ± 0.13	1.80 ± 0.17	0.48 ± 0.11	0.63 ± 0.16	1.97 ± 0.77
Cerebral Peduncle	Normal	0.78 ± 0.04	0.82 ± 0.07	1.71 ± 0.17	0.37 ± 0.06	0.38 ± 0.02	3.25 ± 0.63
	Ventriculomegaly	0.74 ± 0.05**	0.92 ± 0.08**	1.89 ± 0.15**	0.37 ± 0.05	0.39 ± 0.03	4.20 ± 1.09*
	Combined	0.77 ± 0.05	0.85 ± 0.07	1.80 ± 0.17*	0.37 ± 0.06	0.39 ± 0.02	3.87 ± 1.16
External Capsule	Normal	0.72 ± 0.03	0.83 ± 0.09	1.62 ± 0.15	0.44 ± 0.07	0.33 ± 0.02	2.24 ± 0.71
	Ventriculomegaly	0.67 ± 0.05	0.88 ± 0.06	1.69 ± 0.12	0.47 ± 0.07	0.34 ± 0.02	1.92 ± 0.83
	Combined	0.69 ± 0.04	0.85 ± 0.08	1.65 ± 0.14	0.45 ± 0.07	0.33 ± 0.02	2.10 ± 0.58
Optic Tract	Normal	0.79 ± 0.04	0.85 ± 0.07	1.83 ± 0.13	0.36 ± 0.06	0.24 ± 0.03	3.46 ± 0.65
	Ventriculomegaly	0.77 ± 0.04	0.92 ± 0.06*	2.02 ± 0.16**	0.38 ± 0.06	0.25 ± 0.02	4.69 ± 1.18
	Combined	0.78 ± 0.04	0.88 ± 0.09	1.91 ± 0.18*	0.36 ± 0.07	0.25 ± 0.03	3.76 ± 1.33
Striatum	Normal	0.37 ± 0.08	0.81 ± 0.07	1.08 ± 0.13	0.67 ± 0.05	0.31 ± 0.03	2.89 ± 0.82
	Ventriculomegaly	0.31 ± 0.04**	0.86 ± 0.08*	1.22 ± 0.19**	0.68 ± 0.06	0.31 ± 0.04	3.50 ± 1.26
	Combined	0.34 ± 0.07*	0.83 ± 0.08	1.14 ± 0.17	0.68 ± 0.05	0.32 ± 0.03	3.07 ± 1.12
Cortex	Normal	0.33 ± 0.04	0.80 ± 0.06	1.08 ± 0.13	0.67 ± 0.05	0.38 ± 0.03	1.71 ± 0.56
	Ventriculomegaly	0.31 ± 0.02	0.87 ± 0.08**	1.22 ± 0.19**	0.72 ± 0.06**	0.36 ± 0.03	1.46 ± 0.44
	Combined	0.32 ± 0.03	0.83 ± 0.07	1.12 ± 0.10	0.69 ± 0.06	0.37 ± 0.03	1.60 ± 0.65

FA, fractional anisotropy; MD, mean diffusivity; $\lambda_{\parallel}$, parallel diffusivity; $\lambda_{\perp}$, perpendicular diffusivity.

Data are presented (mean ± SD) for normal and ventriculomegaly rat groups, and for all rats (Combined).

p-values for ventriculomegaly and combined groups are vs. the normal group.

*
p<0.05

** $p<0.01$.